NANOROBOTS

Modular reconfiguration of DNA origami assemblies using tile displacement

Namita Sarraf[1], Kellen R. Rodriguez[2,3,4], Lulu Qian[1,4]*

The power of natural evolution lies in the adaptability of biological organisms but is constrained by the time scale of genetics and reproduction. Engineering artificial molecular machines should not only include adaptability as a core feature but also apply it within a larger design space and at a faster time scale. A lesson from engineering electromechanical robots is that modular robots can perform diverse functions through self-reconfiguration, a large-scale form of adaptation. Molecular machines made of modular, reconfigurable components may form the basis for dynamic self-reprogramming in future synthetic cells. To achieve modular reconfiguration in DNA origami assemblies, we previously developed a tile displacement mechanism in which an invader tile replaces another tile in an array with controlled kinetics. Here, we establish design principles for simultaneous reconfigurations in tile assemblies using complex invaders with distinct shapes. We present toehold and branch migration domain configurations that expand the design space of tile displacement reactions by two orders of magnitude. We demonstrate the construction of multitile invaders with fixed and variable sizes and controlled size distributions. We investigate the growth of three-dimensional (3D) barrel structures with variable cross sections and introduce a mechanism for reconfiguring them into 2D structures. Last, we show an example of a sword-shaped assembly transforming into a snake-shaped assembly, illustrating two independent tile displacement reactions occurring concurrently with minimum cross-talk. This work serves as a proof of concept that tile displacement could be a fundamental mechanism for modular reconfiguration robust to temperature and tile concentration.

INTRODUCTION

Modular robots made of self-reconfigurable components provide potential opportunities for adaptive behaviors in complex operating environments (*1*). The principle of modular self-reconfiguration will particularly benefit the development of molecular robotic systems because their ability to handle unforeseen situations during autonomous operation is highly desired—imagine an artificial cell that reconfigures into different forms in response to a changing molecular environment, undergoing fast self-reprogramming within the lifetime of the synthetic organism. DNA origami (*2*) has been used to build modular components for molecular robots, for example, in creating programmable mechanical motion (*3*, *4*), assembly and disassembly of multistate complex structures (*5*), filaments with robotic arms at probabilistically controlled distance (*6*), and a printer-like apparatus for dynamic positioning and patterning (*7*). Moreover, the addressability of DNA origami has been exploited to provide spatial organization for molecular information-processing circuits (*8*) and motors (*9*–*12*), in theory enabling parallel and scalable computation using a small and constant set of unique molecules (*13*). Combining the modularity and addressability, let us envision an artificial cell whose membrane is made of hundreds to thousands of DNA origami tiles (*14*); each tile has a distinct circuit or group of motors attached to the outer or inner side of the membrane, such that the global function of the cell signaling processes is determined by the connectivity of the circuits and motors through neighboring tiles (*15*). Stimuli-responsive self-reconfiguration of the tile assembly would result in functional changes of the information-processing machinery of the artificial cell, allowing it to adapt from one form to another when the collective effect of the changes becomes substantial.

Toward modular self-reconfiguration in DNA origami assemblies, we developed a tile displacement mechanism for controlling dynamical interactions between DNA origami tiles (*16*), analogous to the strand displacement mechanism for controlling the dynamical interactions between small DNA strands (*17*). In a strand displacement reaction, an invader strand binds to a double-stranded complex via a short toehold domain. Branch migration occurs when two strands compete to bind to the same complementary strand until the previously bound strand is released and the invader strand becomes bound instead. Tile displacement follows the same abstract principle but occurs at a larger scale between interacting DNA origami tiles. The complementarity between tiles can be encoded in both the shapes of tile edges (*18*, *19*) and the sequences of short sticky ends (*14*, *15*). Unlike tile assembly and disassembly, tile displacement allows for sequestered domains on tile edges to be activated only upon the arrival of invader tiles, which is key for cascading of reactions that could lead to complex network behaviors and for the kinetics of reactions to be controlled by the strength of the toehold domains (*16*).

Experimental demonstration of tile displacement systems has so far been limited to simple logic and swap behaviors in arrays of up to three by three in size, where the initial and final structures were of the same shape and the invader structures consisted of one or two tiles (*16*). Here, we establish design principles for more complex reconfigurations. We investigate the design space and robustness of tile displacement with varying domain types, toehold properties, and edge identities. We explore the challenges for assembling

[1]Bioengineering, California Institute of Technology, Pasadena, CA 91125, USA. [2]Business Economics and Management, California Institute of Technology, Pasadena, CA 91125, USA. [3]Astrophysics, California Institute of Technology, Pasadena, CA 91125, USA. [4]Computer Science, California Institute of Technology, Pasadena, CA 91125, USA.
*Corresponding author. Email: luluqian@caltech.edu

multitile invaders and develop design principles for improving their yield. We show how to construct invaders with variable sizes, to grow barrels, and to open up three-dimensional (3D) barrels into 2D structures via tile displacement. We further demonstrate two functionally independent tile displacement reactions occurring simultaneously, initiated by two invaders of distinct shapes.

Components of the system shown in Fig. 1 will be used as a running example in this work. Four types of tiles were designed to self-assemble into a seven-tile sword structure. Two invaders were designed, one of which reconfigures the blade of the sword into a snake tail and the other of which reconfigures the handle of the sword into a snake head. Two open toeholds in the sword are located on either side of the center tile connecting the blade and handle. A toehold domain typically consists of two to four edge staples that each provides a stacking bond and a 2-nucleotide (nt) sticky end. An invader (for example, tail or head) binds to an open toehold, and subsequent branch migration occurs perpendicular to the direction of adjacent DNA helices when two tile edges (for example, brown or yellow) compete for binding to their complementary edge until the previously bound structure (for example, blade or handle) is released. Although only the center tile is shared between the sword and snake structures, the reconfiguration process refers to the system-level change from the three initial structures (sword, tail, and head) to the three final structures (snake, blade, and handle). In general, in a tile displacement process, weak interactions between edge staples are important for allowing breathing, which is a condition for branch migration; structural flexibility of the tile is important for allowing competition between an invader and a previously bound structure, because they both need to bend out of the way when branch migration proceeds.

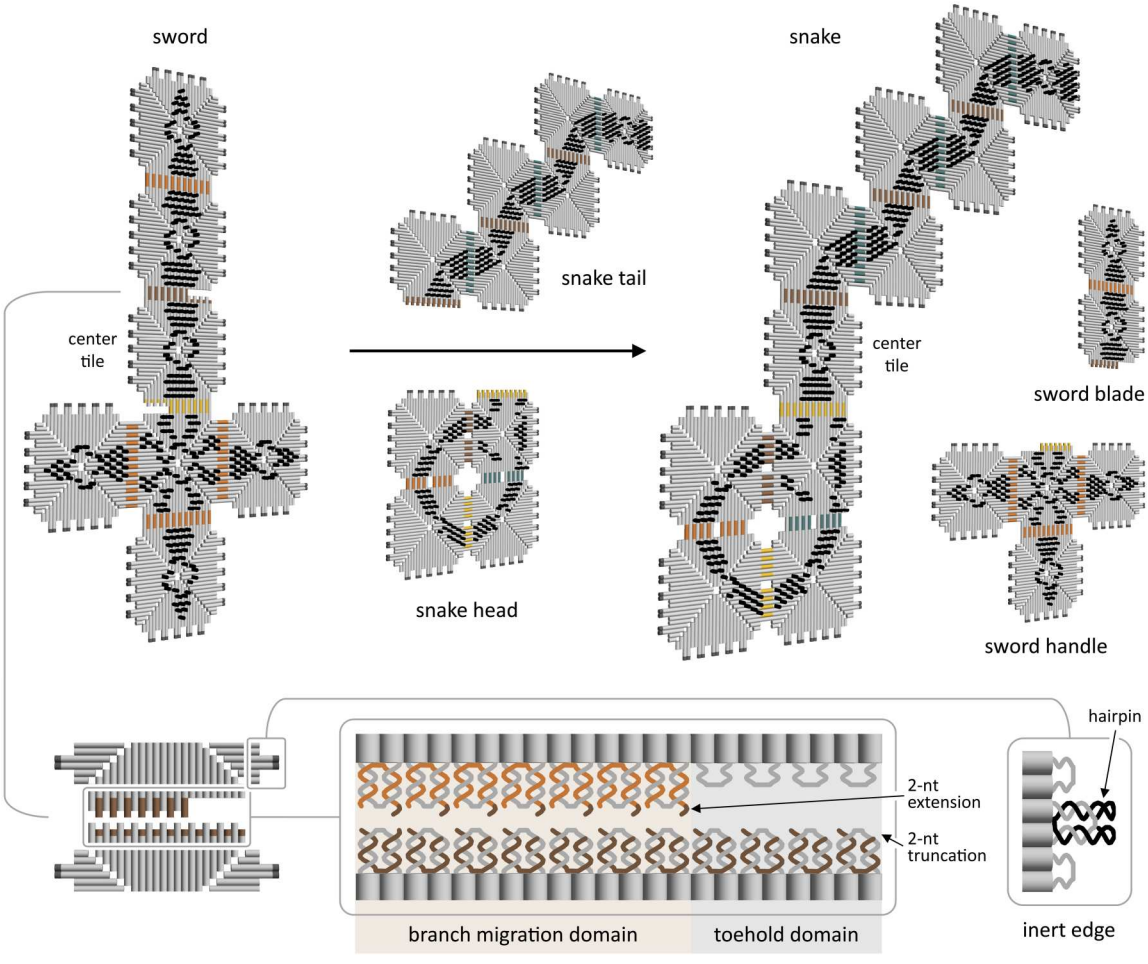

Fig. 1. Design of a sword-shaped assembly reconfiguring into a snake-shaped assembly. Each DNA origami tile is indicated as a square composed of four triangles; each cylinder in the triangle indicates a double helix. Black dots on tile surfaces indicate staple extensions of 20 base pairs, providing patterned contrast in AFM images. Each of the four tile edges consists of up to 11 edge staples. The toehold and branch migration domains shown here consist of four and seven edge staples, respectively, each of which has a stacking bond and a 2-nt sticky end. DNA sequences of the sticky ends determine the identity of the domains, indicated by distinct colors. Complementary domains with matching extensions and truncations in edge staples are shown in the same color. Inert tile edges consist of five edge staples that each have two hairpins for covering up the stack bonds.

RESULTS

Design space and robustness

To understand the design space of tile displacement reactions, we considered the simplest case where a cover tile (CT) and a base tile (BT) formed a dimer (CT:BT), which had an open toehold that allowed an invader tile (Inv) to displace the cover and form an invader-base dimer (Inv:BT). There were two possible types of toehold and branch migration domains: "giving" and "receiving" domains that consisted of staples with extensions and truncations, respectively. In our previous study, the kinetics of tile displacement was quantified for invaders with a "giving toehold" and a "giving branch migration domain" (*16*). With this configuration, given four unique tile edges that have distinct sets of staple sequences and two ways of creating matching staple extensions and truncations (5′ extension and 3′ truncation versus 3′ extension and 5′ truncation), a total of eight unique tile displacement reactions can be designed. This analysis of the design space was under the conditions that the sticky end sequences were fully determined by the scaffold sequence and that the same 5′ or 3′ choice of staple extension was applied to an entire edge. Sticky ends could be designed on the basis of staple-staple interactions (*14*), but the stacking bonds would be sacrificed, and the length of the sticky ends would be constrained by the nearest staple and scaffold crossover locations.

Here, we investigated all four giving and receiving combinations of toehold and branch migration domains in an invader tile (Fig. 2A). To measure the kinetics of these tile displacement reactions, we modified a pair of edge staples located at the end of the branch migration domain opposite from the toehold with a fluorophore and a quencher. The modified edge staples did not have any sticky ends so that they can be used in a variety of fluorescence experiments regardless of the tile design. The effective rate (k) of tile displacement was estimated by comparing simulation with fluorescence kinetics data (Fig. 2B). In all four cases, the rates were within roughly threefold of each other. In G-R (giving toehold and receiving branch migration) and R-G (receiving toehold and giving branch migration) configurations, the toehold and branch migration domains may have different edge identities (indicated as distinct colors) because the truncated staples in these domains are located on two different tile edges. Thus, a given branch migration domain can be composed together with four distinct toehold domains. Moreover, in these two configurations, a toehold on the left or right side of the edge results in two distinct invaders. Combining the two possibilities, eight times more unique reactions can be designed for G-R and R-G edges than for G-G and R-R edges. With all four domain combinations, the design space was therefore increased from 8 to 144 unique tile displacement reactions (fig. S4A).

Next, we investigated whether a toehold can be composed of staples that are separated by branch migration domains (Fig. 2C). Fluorescence kinetic experiments suggested that the kinetics of tile displacement with a discontinuous toehold is similar to that with a continuous toehold (Fig. 2D). A discontinuous toehold is conceptually similar to mismatch elimination in strand displacement (*20*). For example, the discontinuous toehold in Fig. 2C can be seen as one toehold staple and two mismatch staples in the branch migration domain on the cover:base dimer (CT:BT). However, in strand displacement, moving a nucleotide from an open toehold to a mismatch in the branch migration domain results in slower kinetics unless the mismatch position is close to the toehold. We had two explanations for why the observation was different in tile displacement. First, an origami tile edge is more rigid than a single strand of DNA; once a pair of complementary edge staples bind, other staples on the same edge can line up with little entropic cost. Second, a toehold staple on the BT has its complementary staple removed from the CT, which leaves a relatively large space (about 6 nm wide and 6 nm tall) for an invader to bind even when a toehold staple is flanked by two branch migration staples. With discontinuous toeholds, instead of placing a toehold on the left or right side of an edge, there were 17 possible toeholds [based on a known function in coding theory (*21*)] consisting of 3 of the 11 edge staples, in which any two toeholds shared at most one common staple—this allowed the design space to further increase from 144 to 1104 unique tile displacement reactions (fig. S4B).

Naturally, not all of the above reactions could be used in one tile displacement system without any concerns of spurious interactions such as cross-talk or occlusion. Analysis at the sequence level could be performed to inform the design. Here, we identified one type of spurious interaction just on the basis of the edge identities. As discussed earlier, staples on one edge can be extended with sticky end sequences that are complementary to the scaffold sequence on any of the four tile edges. The identity of an edge x giving to edge y is referred to as ExGy, where $x, y \in \{1, 2, 3, 4\}$ (Fig. 2E and fig. S3). We showed that the kinetics of tile displacement was substantially (30 times) slower when $x = y$ in the invader (Fig. 2F). This is likely because the invader occludes itself by reversibly forming dimers via spurious branch migration at the strand level between all pairs of staples along the edge (Fig. 2G). Compared with reversible invader dimerization, irreversible binding between an invader and BT is much favored, and thus, tile displacement was still able to take place despite the slower kinetics. To maintain a regular tile displacement rate, self-occluding edges (ExGx) should be avoided in future designs, which brings down the number of unique tile displacement reactions from 1104 to 832 (fig. S4C).

To summarize, using different types of toehold and branch migration domains (G-R and R-G) increased the design space of tile displacement reactions by roughly an order of magnitude, whereas exploiting discontinuous toeholds further increased the design space by another order of magnitude (Fig. 2H). The reaction kinetics was fairly robust to varying domain types and toehold properties so long as self-occluding edges were avoided. Even without using rationally designed sticky end sequences and just relying on the natural sequence of M13 scaffold, the design space is large enough for complex system behavior involving hundreds of distinct reactions. If desired, a larger sequence space could be achieved by exploiting different permutations of the circular M13 strand (*22*, *23*) at the cost of additional sets of staples. Alternatively, extending the tile edges with helper strands [referred to as extended edges (*15*)] would allow for a cost-effective solution for arbitrary sticky end sequences.

Yield of assemblies

Knowing that self-occluding edges slow down the kinetics of tile displacement, we sought to understand their effect on the yield of tile assembly. We compared two designs of a sword-shaped structure assembled from tiles with and without self-occluding edges (Fig. 3, A and C). Atomic force microscopy (AFM) images showed more incomplete structures and aggregations for the

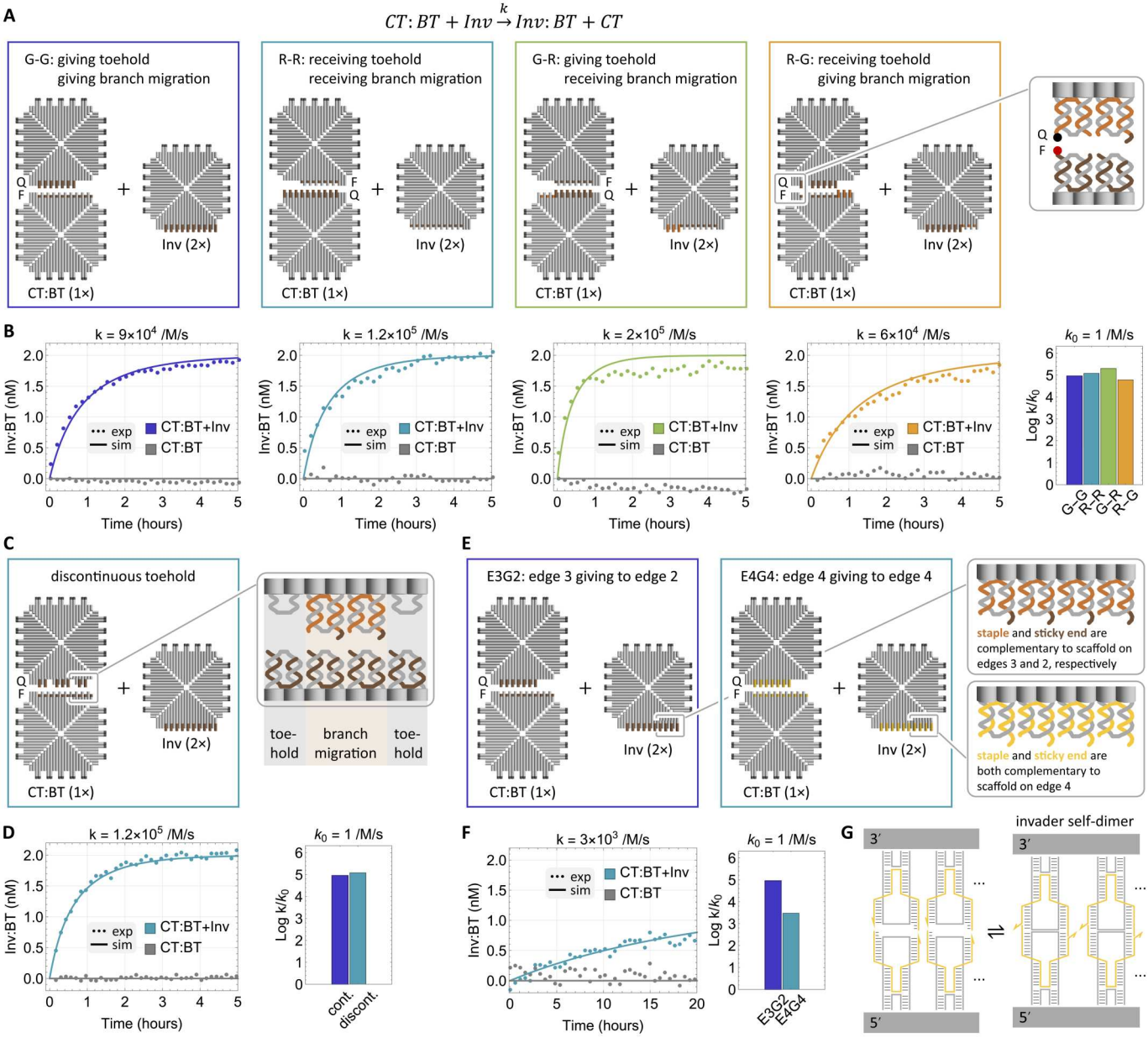

H

Domain type (toehold-branch migration)				Toehold property		Edge identity (ExGy)		Number of reactions
G-G	R-R	G-R	R-G	continuous	discontinuous	$\forall x, y$	$x \neq y$	
✓				✓		✓		8
✓	✓	✓	✓	✓		✓		144
✓	✓	✓	✓		✓	✓		1104
✓	✓	✓	✓		✓		✓	832

Fig. 2. Design space and robustness of tile displacement reactions. (**A**) Designs of invaders with four combinations of giving or receiving toehold and branch migration domains. Cover, base, and invader tiles are indicated as CT, BT, and Inv, respectively. Fluorophore and quencher are indicated as F and Q, respectively. (**B**) Simulation and fluorescence kinetics data for various domain types. (**C**) Design with toehold staples separated by other staples in the branch migration domain. (**D**) Simulation and fluorescence kinetics data for the discontinuous toehold. (**E**) Designs with toehold and branch migration domains giving to a different or the same tile edge. (**F**) Simulation and fluorescence kinetics data for E4G4. (**G**) Spurious strand displacement leading to an invader self-dimer. (**H**) Numbers of distinct tile displacement reactions with various domain types, toehold properties, and edge identities. In (B), (D), and (F), experiments were performed at 25°C with standard concentration 1× = 2 nM. Simulations and experiments are shown in solid and dotted trajectories, respectively. Estimated rate constants are shown in logarithmic scale. Design and results of the continuous toehold and E3G2 are the same as the G-G invader.

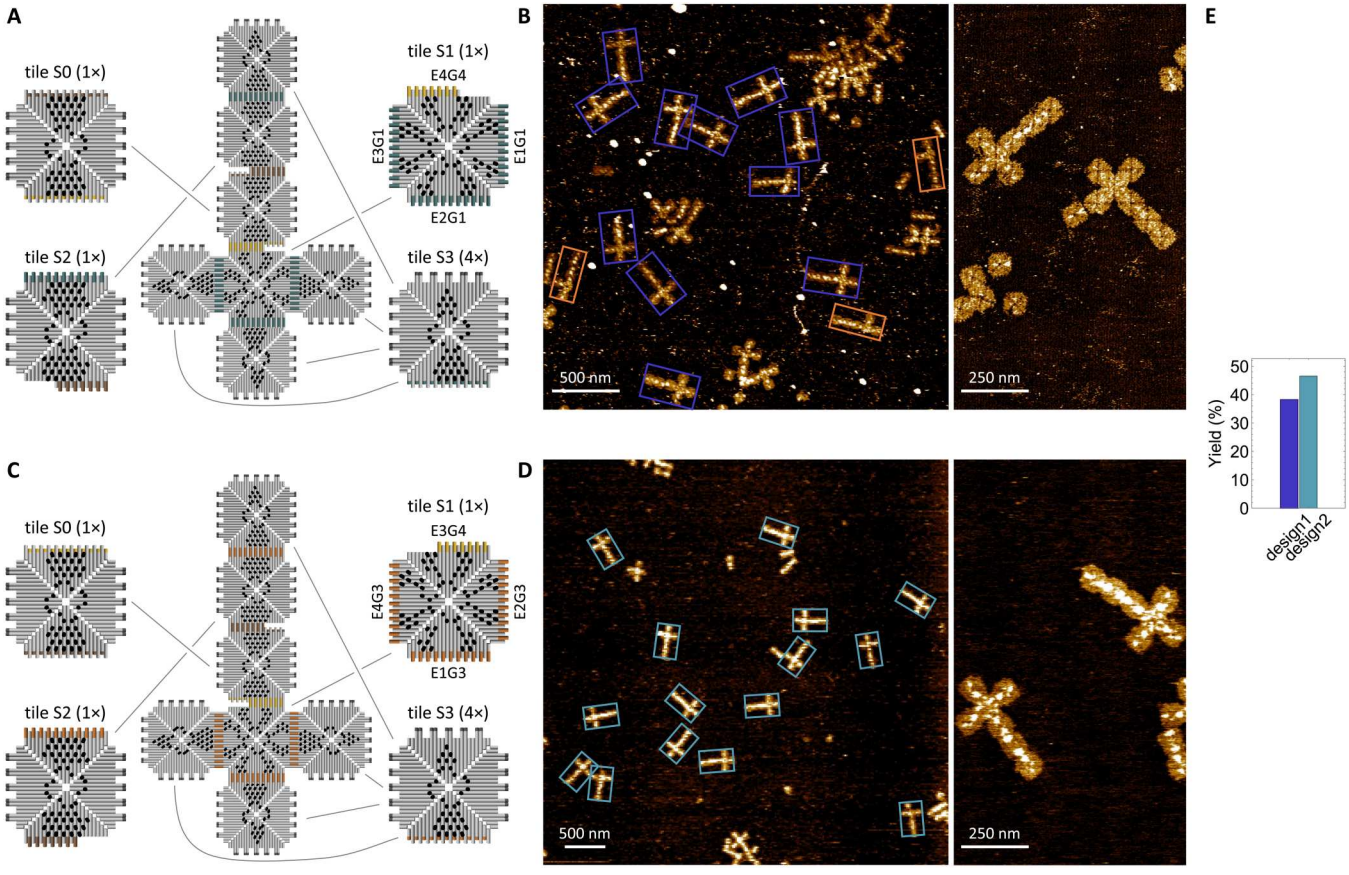

Fig. 3. Improving the yield of tile assembly by avoiding self-occluding edges. (**A** and **B**) Design (A) and AFM images (B) of a sword shape self-assembled from tiles that have self-occluding edges (design1). (**C** and **D**) Design (C) and AFM images (D) of a sword shape self-assembled from tiles that do not have self-occluding edges (design2). (**E**) Estimated yields of sword assemblies with the two designs. The yield was estimated using 10 μm–by–10 μm AFM images containing at least one hundred structures (fig. S10). 1× = 6 nM. Complete and incomplete structures are highlighted with distinct colors.

design with self-occluding edges (Fig. 3, B and D). For example, a noticeable population of incomplete structures was the one-armed sword (highlighted in orange boxes in Fig. 3B). The open (that is, noninert) edge in the one-armed sword corresponded to the E1G1 edge on tile S1 (fig. S5A), compatible with the hypothesis that the self-occluding edge might have resulted in reversible dimerization of two copies of tile S1, preventing tile S3 from fully incorporating into the sword. Another self-occluding edge, E4G4 on tile S1, had 7 instead of 11 edge staples and showed less effect on the yield of assembly (less corresponding incomplete structures observed in AFM images). Overall, an 8.3% increase in yield was observed for the design without self-occluding edges (Fig. 3E).

A challenge for the assembly of multitile invaders was the competition between internal and external edges. For example, in the snake head invader shown in Fig. 4A, one of the three active edges on tile H1 (colored in yellow) was located at the exterior of the assembly and was used to initiate tile displacement for reconfiguring the sword handle. Because all four edge identities had been used in the internal edges of the invader to form a two-by-two structure, the active external edge happened to be complementary to a receiving edge on tile H2. During the annealing process used for tile assembly, the cooperative binding between two tile edges was expected to encourage the formation of the two-by-two structure at a higher temperature. The undesired interaction between tiles H1 and H2 was expected to occur at a lower temperature; if the tiles were used up by then, there would be few undesired structures. However, AFM images showed many undesired structures containing five or more tiles (highlighted in orange boxes in Fig. 4B). The yield of the head invader was estimated to be 62.8% (Fig. 4E), which was 30% lower than the yield of two-by-two arrays with inert external edges (*24*).

An explanation of the relatively low yield was that the undesired binding between tiles H1 and H2 was too strong (fig. S7). Although the melting temperature of the desired invader structure (T_2) was supposed to be notably higher than the melting temperature of the undesired assembly (T_1), the annealing process can only start at a temperature (for example, T_0 = 50°C) below the melting temperature of the DNA origami tiles. If $T_2 > T_0$, then the gap between T_1 and T_0 effectively determines the yield of the invader. For the external edge to participate in tile displacement, it had to include a toehold and a branch migration domain, which essentially required a full set of 11 edge staples. Thus, reducing the strength of the external edge was not a good option here. Given these considerations, we sought to reduce the strength of the internal edges, which would reduce both T_2 and T_1, because the undesired binding involved an internal and an external edge. As long as T_2

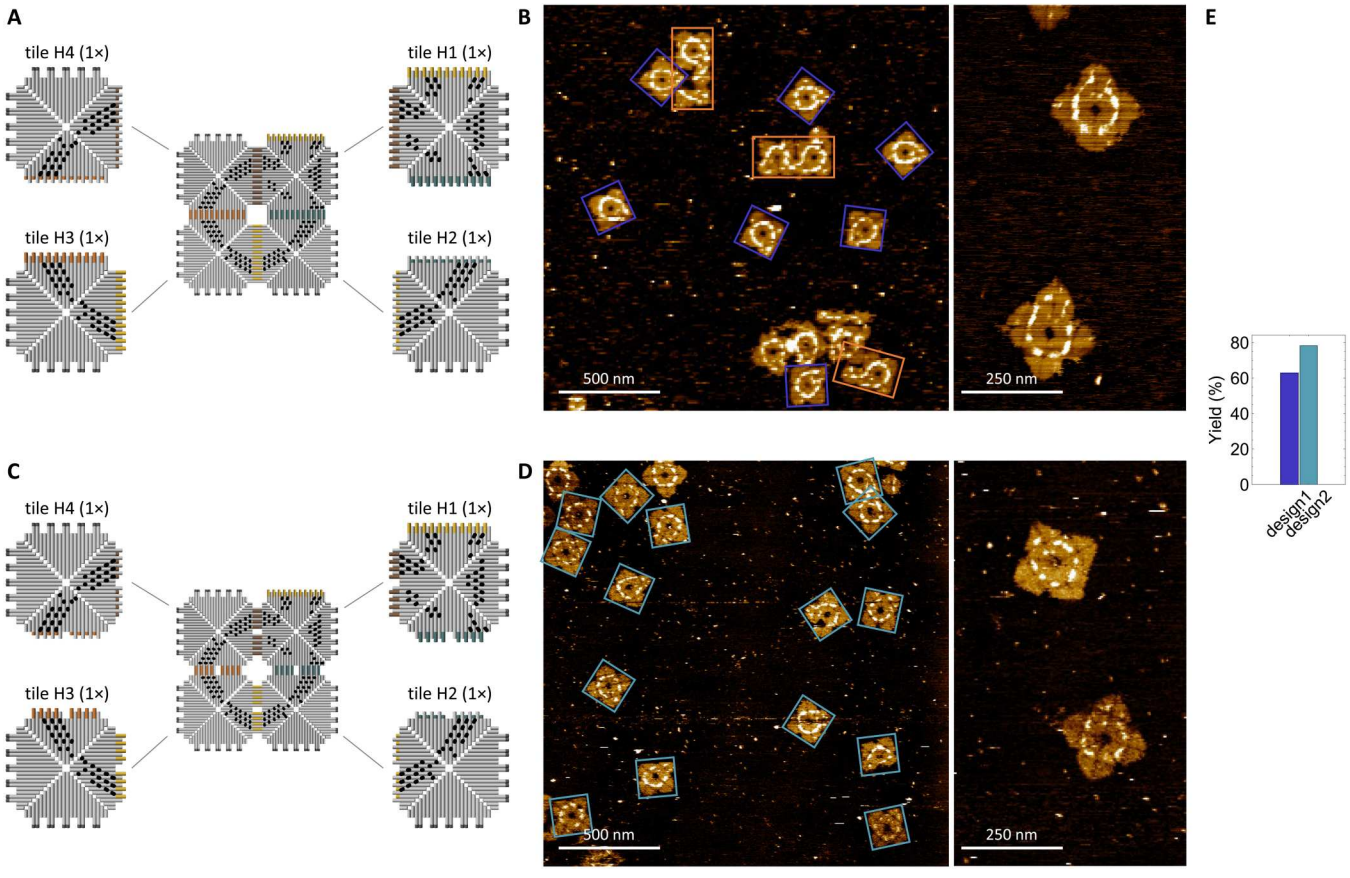

Fig. 4. Improving the yield of a multitile invader. (**A** and **B**) Design (A) and AFM images (B) of a head invader with the same number of staples on the external and internal edges (design1). (**C** and **D**) Design (C) and AFM images (D) of a head invader with a reduced number of staples on the internal edges (design2). (**E**) Estimated yields of head invaders with the two designs. The yield was estimated using 10 μm–by–10 μm AFM images containing at least a hundred structures (fig. S11). 1× = 10 nM. Desired and undesired structures are highlighted with distinct colors.

remained greater than or equal to T_0, the yield would benefit from the decrease in T_1. With three edge staples removed from each of the internal edges (Fig. 4C), after which $T_2 \approx 52$°C (*24*), substantially fewer undesired structures were observed in AFM images (Fig. 4D), and the yield of the head invader was improved to 78.2% (Fig. 4E).

Other design changes could be explored to reduce the competition between internal and external edges on multitile invaders, for example, using a 3′ staple extension on internal edges and a 5′ staple extension on external edges. Nonetheless, we showed that a simple design principle that adjusted the number of staples on internal edges to increase the gap between the starting temperature of annealing and the melting temperature of undesired tile assembly helped increase the yield without requiring an additional set of edge staples.

Invaders with variable sizes

The snake tail invader served as a good example to understand how to control the size distribution of DNA origami tile polymers. The invader consisted of three types of tiles: *a*, *b*, and *c* (Fig. 5A). Tiles *a* and *b* were designed to grow into polymers with a zigzag shape, whereas tile *c* was designed to cap the growth. Naturally, the ratio of these tiles can be used to control the length distribution of the polymers. First, a lower tile ratio c:$(a + b)$ was expected to result in longer polymers. Second, assuming that all polymers end with tile *c*, the tile ratio a:b was expected to determine whether polymers starting with tile *a* or *b* were favored. Specifically, a:$b = (n + 1)$:n was expected to favor even-length polymers starting with tile *a*, and a:$b = n$:n was expected to favor odd-length polymers starting with tile *b* (fig. S12). Because tile *a* had an edge to initiate tile displacement for reconfiguring the sword blade, even-length polymers were desired here. Thus, we used a tile ratio of a:b:$c = (n + 1)$:n:1 for growing the snake tail invader, where $n = 1$ and 2 were used for growing a shorter and longer tail, respectively.

We developed a model to simulate the polymer growth. Reactions can be enumerated on the basis of a defined set of monomers, assembly rules, assembly rates, and a maximum polymer length (Fig. 5B). Each assembly rule was specified as a pair of monomers that can bind to each other in a particular order (left to right or bottom to top, as two alternating directions in a zigzag polymer). The rules were asymmetric. For example, {*a*, *b*} was not equal to {*b*, *a*}, indicating that tile *a* could bind to the left or top of tile *b*, respectively. Each assembly rate mapped to an assembly rule, specifying the bimolecular rate constant of tile binding. Here, we assumed that all rates were the same, using the value from a previous study (*16*). We also assumed that the reactions were irreversible,

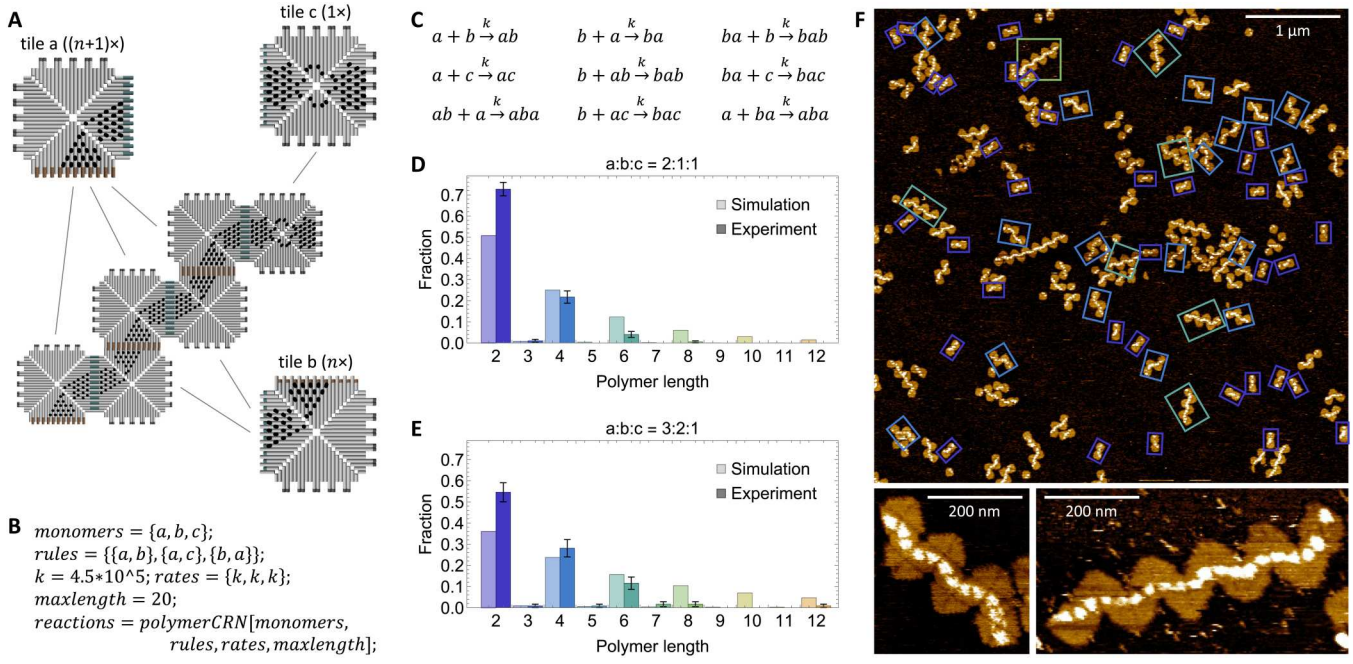

Fig. 5. Controlling the length distribution of polymers with tile ratios. (**A**) Design of a tail invader with variable length. (**B**) Enumerating the reactions with defined monomers, assembly rules, assembly rates, and maximum polymer length. The unit of k is per molar per second. (**C**) An example set of nine reactions enumerated with maxlength = 3. (**D** and **E**) Simulation and experimental data of polymer length distribution with tile ratio *a*:*b*:*c* = 2:1:1 (D) and 3:2:1 (E). For simulation, each fraction was calculated as $c_i/\Sigma c_i$, where c_i is the concentration of polymer of length i. For experimental data, each fraction was calculated as $n_i/\Sigma n_i$, where n_i is the number of polymers of length i in two 5 μm–by 5 μm AFM images (fig. S13). The standard error (SE) was calculated as $\sqrt{p(1-p)/n}$, where p is the fraction and n is the total number of polymers, treating the fraction as a Bernoulli probability. n = 198 and 121 for *a*:*b*:*c* = 2:1:1 and 3:2:1, respectively. (**F**) AFM images of tile assemblies with *a*:*b*:*c* = 3:2:1. Structures that contain a single copy of tile *c* but varying copies of tiles *a* and *b* are highlighted with distinct colors. 1× = 13.5 and 9 nM for *a*:*b*:*c* = 2:1:1 and 3:2:1, respectively.

given that the tile binding was sufficiently strong. Modeling them as reversible reactions that allow for polymers to break apart does not have a substantial effect so long as the growth remains much faster than the breakage. An experimental system does not have a set maximum length of polymers, and polymers could grow infinitely. Setting a maximum length in simulation allowed for the system behavior to be approximated by a finite chemical reaction network. Empirically, a good choice for the maximum length is just large enough that no noticeable changes in the simulation are observed with a larger number.

For example, with the three types of monomers and three assembly rules shown in Fig. 5B, a total of nine reactions were enumerated when maxlength = 3 (Fig. 5C). The following simulations were performed with maxlength = 20, where 570 reactions were enumerated and then simulated with mass-action kinetics using the CRN Simulator (*25*). When *a*:*b*:*c* = 2:1:1, the concentrations of odd-length polymers were about zero, whereas the concentrations of even-length polymers decreased exponentially with their length (Fig. 5D). When *a*:*b*:*c* = 3:2:1, the same phenomena were observed in simulation, but the concentrations of shorter polymers (length $\leq$ 4) decreased, whereas those of longer polymers (length $\geq$ 6) increased (Fig. 5E). Experimental data semiquantitatively agreed with the simulations (Fig. 5, D and E).

AFM images showed that even-length polymers were dominant in structures that contained a tile *c* (Fig. 5F). However, roughly 50% of the structures contained just tiles *a* and *b*, contradictory to the simulation prediction that the concentrations of *ab*-only polymers should be about zero. This observation prompted us to explore the formation of 3D tile assemblies and their reconfiguration through tile displacement.

Barrels and their reconfiguration

It is known that DNA origami tiles can bend along the seams where staples containing single-stranded domains are used to bridge adjacent helices at an angle (for example, 90° angle between helices in adjacent triangles composing the square tile); this bending encourages the formation of 3D structures, for example, as seen in a spherical structure composed of 20 triangular tiles (*22*). We thus hypothesized that *ab* polymers can form 3D barrel-like structures, which would then be flattened and broken open on a mica surface during AFM imaging. For example, polymer *abab* or *ababab* could form a barrel with a square- or hexagonal-shaped cross section by 90° or 60° bending along the diagonals of the tiles, respectively (Fig. 6A). Once the polymers have closed up into barrels, no tile *c* can further bind to the assemblies. This hypothesis also explained why there was a larger population of *ac* observed in the AFM images than predicted by simulation (Fig. 5, D and E): Reactions like *abab* + *ac* → *ababac* would be unable to take place if polymers like *abab* formed barrel structures.

To investigate this hypothesis, we annealed tiles *a* and *b* at a 1:1 ratio and then added tile *c* to the mixture. In AFM images of the assemblies before tile *c* was added, tiles *a* and *b* commonly appeared in a polymer or a small cluster of tiles and polymers (Fig. 6C). We suspected that this was because when a barrel was flattened on mica, one or more locations between tiles could be broken open, resulting in a single structure or multiple pieces of a structure. Once

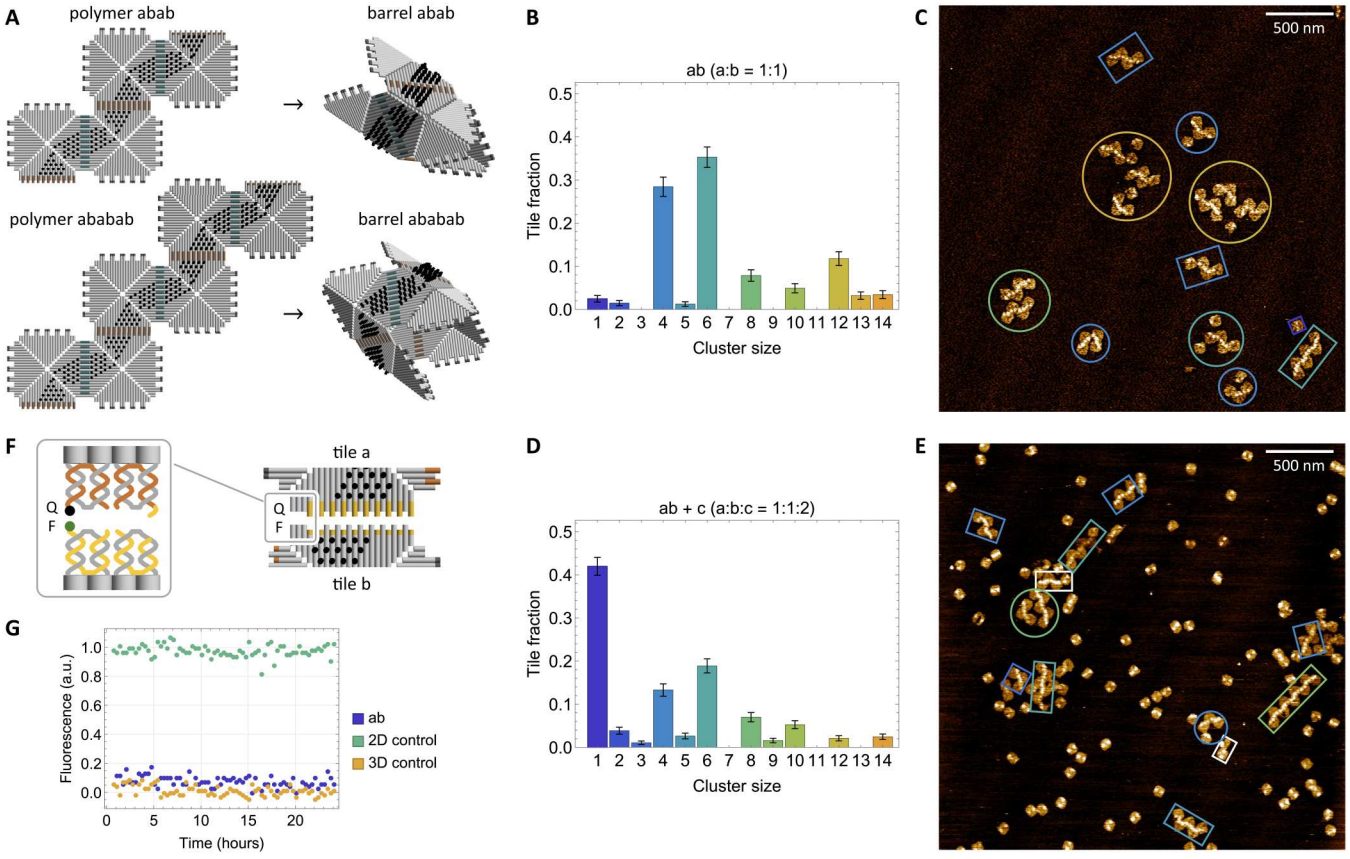

Fig. 6. Verifying the formation of barrels. (**A**) Two example barrel structures formed from polymers of lengths 4 and 6, respectively. (**B** and **C**) Size distribution (B) and AFM image (C) of structures assembled from tiles *a* and *b* at 5 nM. (**D** and **E**) Size distribution (D) and AFM image (E) of structures assembled from tiles *a*, *b*, and *c*, whereas tile *c* at 10 nM was added after 24 hours. Each tile fraction was calculated as $n_i \times i/\Sigma(n_i \times i)$, where n_i is the number of structures or clusters of structures that contain *i* tiles in a 10 μm–by–10 μm AFM image (fig. S14). The SE was calculated as $\sqrt{p(1-p)/n}$, where *p* is the fraction and *n* is the total number of tiles, treating the fraction as a Bernoulli probability. *n* = 408 and 572 for *ab* and *ab* + *c*, respectively. Structures or clusters of varying sizes are highlighted with rectangles or circles of distinct colors, respectively. (**F**) Quencher- and fluorophore-labeled edge staples in tiles *a* and *b*. (**G**) Fluorescence data of structures self-assembled from tiles *a* and *b* at 2 nM. a.u., arbitrary units.

separated, the pieces can diffuse on mica, especially upon being pushed by an AFM tip during scanning; however, they would typically remain nearby and appear as a small cluster in an image. We counted the size of each structure or a cluster of structures: Most of them contained an even number of tiles, agreeing with the property of the barrels (Fig. 6B). After tile *c* was added, 84% of tile *c* remained as monomers, indicating that they were largely unable to react with the structures self-assembled from tiles *a* and *b*, which agreed with the formation of barrels (Fig. 6D). A representative AFM image is shown in Fig. 6E, where only 2 of the 12 multitile structures or clusters of structures contained a tile *c* (highlighted in white boxes). Comparing the statistics before and after tile *c* was added, the distribution of structures with sizes greater than or equal to 2 remained roughly the same, whereas the number of tiles in these structures (as a fraction of the total number of tiles) differed by roughly twofold because of the addition of tile *c* (Fig. 6, B and D). This observation also suggested that structures containing tiles *a* and *b* were largely unable to react with tile *c*.

We further verified the hypothesis using a second type of experiment. A pair of edge staples in tiles *a* and *b* were modified with a fluorophore and quencher (Fig. 6F), which enabled us to measure the fluorescence signal of the assembled structures (Fig. 6G). Tile *b* alone was used as a 2D control, which corresponded to the maximum fluorescence state. An *ab* dimer with inert external edges was used as a 3D control, which corresponded to the minimum fluorescence state. If the polymers made of tiles *a* and *b* closed up into 3D barrels, then all fluorophores would be adjacent to a quencher and thus result in a low fluorescence state; if the polymers remained as 2D structures, then one fluorophore per structure would not be adjacent to a quencher and thus would result in a higher fluorescence state. By comparing the measurement with the two controls that represent the fluorescence states of bound and unbound edges, the experiment suggested that the edges in the structures were about fully bound, again agreeing with the formation of barrels (Fig. 6G).

Next, we showed that the 3D barrels can be reconfigured to 2D linear chains (that is, polymers) by embedding an open toehold in the complementary edges between tiles *a* and *b* (Fig. 7A). In this case, tile *c* will initiate a displacement reaction that opens up the barrel and simultaneously caps the polymer (for example, *abab* + *c* → *ababc*). Comparing simulation with fluorescence kinetics data, we estimated that the effective rate of tile displacement was about 4.5-fold slower than that in the dimer experiments (Fig. 7B). A possible explanation was that the entropic cost of losing one free

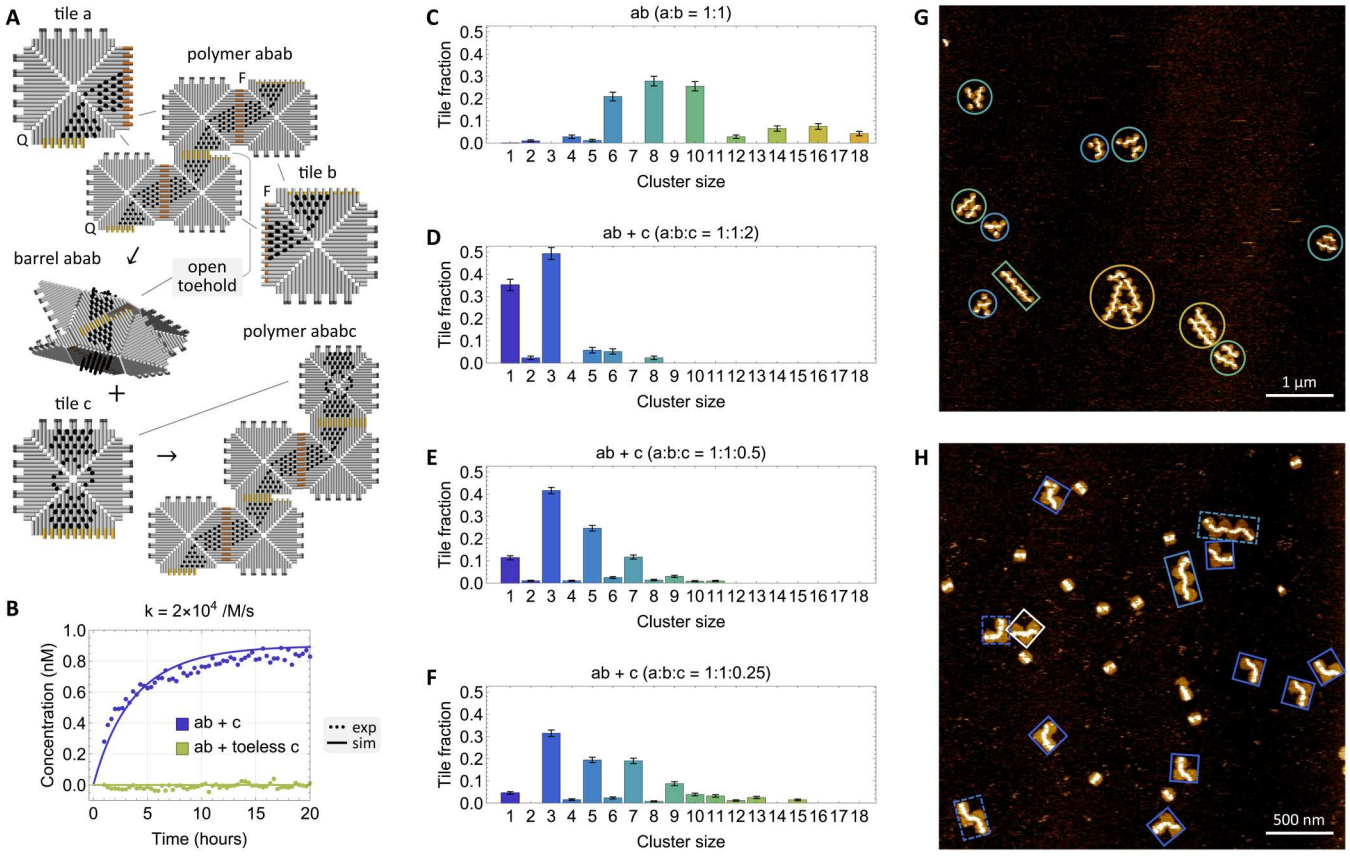

Fig. 7. Reconfiguration of barrels to flat structures. (**A**) A tile displacement reaction that opens up a 3D barrel into a 2D linear chain. (**B**) Fluorescence kinetics data and simulation. Experiments were performed at 25°C with tiles *a*, *b*, *c*, and toeless *c* at 2, 2, 4, and 4 nM, respectively. Simulations and experiments are shown in solid and dotted trajectories, respectively. (**C** to **F**) Size distribution of structures without (C) or with tile *c* added after 24 hours at ratio *a*:*b*:*c* = 1:1:2 (D), 1:1:0.5 (E), or 1:1:0.25 (F). Each tile fraction was calculated as $n_i \times i / \Sigma(n_i \times i)$, where n_i is the number of structures or clusters of structures that contain *i* tiles in three 10 μm–by–10 μm AFM images (fig. S15). The SE was calculated as $\sqrt{p(1-p)/n}$, where *p* is the fraction and *n* is the total number of tiles, treating the fraction as a Bernoulli probability. *n* = 431 for *ab*; *n* = 347, 1196, and 1031 for *ab* + *c* with tile ratios *a*:*b*:*c* = 1:1:2, 1:1:0.5, and 1:1:0.25, respectively. (**G** and **H**) AFM image of structures without (G) or with (H) tile *c* added after 24 hours at ratio *a*:*b*:*c* = 1:1:2. Structures or clusters of varying sizes are highlighted with rectangles or circles of distinct colors, respectively.

molecule (the reaction has two reactants but one product) slowed down the kinetics. It could also be the case that tile displacement in 3D structures was slower than that in 2D structures because of the increased geometrical constraint and reduced degree of structural flexibility during branch migration. A control experiment with a "toeless" tile *c* (first four staples on the right side of the active tile edge removed) showed no fluorescence change over time (Fig. 7B), suggesting that the conversion from polymers to barrels was essentially irreversible and that tile *c* cannot bind to a barrel through disassembly and assembly.

We further analyzed AFM images before and after tile *c* was added. Similar to the statistics shown in Fig. 6B, before tile *c* was added, nearly all structures and clusters contained an even number of tiles (Fig. 7C), consistent with the barrel formation. However, a clear difference was that the dominant population shifted from sizes 4 and 6 to sizes 8 and 10. This is presumably because tile *a* in the first design had a self-occluding edge (fig. S8A), which was avoided in the design for barrels with an open toehold (fig. S9). The larger size of the structures was yet more evidence for the benefit of avoiding self-occluding edges. After tile *c* was added, the dominant population became three-tile structures and excess single tiles (Fig. 7D), consistent with the expected products of the tile displacement reactions when there are more tiles *c* than tiles *a* and *b* (for example, *abab* + *c* → *ababc*, and *ababc* + *c* → *abc* + *abc*). A representative AFM image is shown in Fig. 7H, where 8 of the 10 three-tile structures were recognized as *abc*. Two exceptions were *aba* (highlighted in a white box) and *cbc* (highlighted in a dotted blue box); they might be two pieces of a 3D structure that was at an intermediate state of tile displacement before it was broken open and rearranged on mica.

We expected that reducing the concentration of tile *c* would result in longer polymers after tile displacement. This was observed in AFM experiments with tile ratios *a*:*b*:*c* = 1:1:0.5 and 1:1:0.25 (Fig. 7, E and F). Overall, comparing the distributions before and after tile *c* was added, the number of structures and clusters containing an even number of tiles notably decreased, whereas the number containing an odd number of tiles increased, consistent with the expected sizes of the polymers.

The resulting polymers did not satisfy the design requirement of a tail invader (for example, the exposed tile edge has a branch migration domain but not a toehold) and were not used in the following experiments for demonstrating simultaneous tile displacement.

Instead, the results of barrel formation and reconfiguration provided a general mechanism for creating 3D structures with variable cross sections and for applying tile displacement to enable the conversion from 3D to 2D structures with controlled kinetics and size distribution. The barrel structures could be useful for protecting functional molecules attached to the inner side of the structures, which only become accessible for collectively binding to larger objects when the structures are opened up, for example, as seen in therapeutic nanorobots targeting the cell surface (*26*, *27*).

Simultaneous tile displacement

Last, we showed that the snake head and tail invaders can initiate tile displacement reactions separately or simultaneously. Two distinct fluorophores on the sword located at two opposite sides of the center tile S0 were used to monitor the reaction kinetics (Fig. 8A). When only the head invader was present, fluorescence signal on the handle side (TYE563) went high and that on the blade side (ROX) remained low, indicating displacement of the handle but not the blade (Fig. 8B). Similarly, when only the tail invader was present, fluorescence signal on the blade side (ROX) went high and that on the handle side (TYE563) remained low, indicating displacement of the blade but not the handle (Fig. 8C). The effective rate of tile displacement was roughly one-third or two-third of that in the dimer experiments, possibly because of the increased structural complexity of the invaders. That the tail invader was faster than the head invader could just be an effect of the different stacking bonds and sticky end sequences on the two tile edges, or it could also be affected by the different shapes of the invaders. For example, stronger sequences in the toehold could result in faster kinetics, whereas stronger sequences in the branch migration domain could result in slower kinetics. In terms of shape differences, a stronger connectivity among neighboring tiles could result in slower kinetics. For example, the tiles in the tail invader were bound to each other by one edge, whereas the tiles in the head invader were bound to each other by two edges; the reduced degree of freedom in the head invader might have caused branch migration to be slower.

When the head and tail invaders were both present, two fluorescence signals went high, indicating simultaneous displacement of the blade and handle (Fig. 8D). The effective rates of the two tile displacement reactions were a bit slower than when they were measured separately. We suspected that it was due to the two invaders occluding each other and the product of one tile displacement reaction occluding the invader of the other. Because using the M13 scaffold sequence did not allow for sequence optimization such as using a three-letter code (*28*), it was expected that tile assemblies with active external edges could occlude each other via spurious binding.

All populations of structures with designed shapes and patterns were observed in AFM images, including reactants, intermediates, and products of the two tile displacement reactions. When only the head invader was present, AFM images showed two products (head-blade and handle) of similar numbers (Fig. 8E and fig. S17). The unreacted sword was also present. However, the unreacted head appeared to exist largely in aggregates. Because the assembly yield of the sword was relatively low (46.5%, as shown in Fig. 3E), the incomplete structures could have facilitated undesired aggregation. With reduced availability of the head invader, a fraction of the sword would remain unchanged. When only the tail invader was present, AFM images showed two different products (handle-tail and blade) of similar numbers, and there was nearly no unreacted sword (Fig. 8F and fig. S18), suggesting that the incomplete sword structures had much less effect on the tail invader. When both invaders were present, all three products (snake, handle, and blade) were observed (Fig. 8G and fig. S19). Nearly all intermediates seen in the AFM images were handle-tail and not head-blade, consistent with the reduced availability of the head invader. Moreover, structures that looked almost like a snake but lacked the center tile S0 (highlighted in dotted white boxes in Fig. 8G) were evidence of occlusion between the two invaders.

DISCUSSION

We have shown that two methods can substantially increase the design space of tile displacement reactions: (i) using mixed domain types, meaning a giving toehold and receiving branch migration domain or a receiving toehold and giving branch migration domain, and (ii) using discontinuous toeholds, meaning toehold staples intermixed with staples in the branch migration domain. In general, a pair of complementary tile edges can be designed as E*x*G*y* (edge *x* giving to edge *y*) and E*y*R (receiving edge *y*), where $x, y \in \{1, 2, 3, 4\}$. However, we have shown that the kinetics of tile displacement is at least an order of magnitude slower and that the yield of tile assembly is decreased when $x = y$. Edges of the form E*x*G*x* are now identified as self-occluding edges and should be generally avoided in future designs. Furthermore, we have demonstrated that complex, multitile invaders can be constructed with both fixed and variable sizes. Competition between external and internal tile edges during assembly of the invaders must be considered to ensure a sufficiently high yield of desired invader structures. For invaders with variable sizes, ratios of the tile types involved in growing the structure are critical for controlling which tile edge will be exposed for initiating tile displacement, whereas ratios of the tile types involved in capping the growth are critical for controlling the size of the structure. Tile polymers with variable sizes can fold into 3D structures with variable cross sections; by embedding toeholds into these structures, they can be opened up into 2D structures. Building on these design principles, we have demonstrated two independent tile displacement reactions with complex invaders taking place simultaneously in one test tube.

A powerful feature of strand displacement is that it markedly increases the specificity of DNA hybridization (*29*), which allows for systems with hundreds of distinct reactions to be constructed for performing complex molecular information-processing tasks (*30*, *31*). Similar to strand hybridization, binding between DNA tiles has limited specificity. When information processing is solely based on tile assembly and disassembly, the system must operate near its melting temperature (for example, 50°C) to ensure specificity (*32*, *33*). In contrast, we have shown that tile displacement systems operate at room temperature with little cross-talk between distinct reactions. Although only two independent reactions are demonstrated here, it is a proof of concept that tile displacement has the potential to markedly increase the specificity of DNA tile assembly and could serve as a fundamental mechanism for scalable computation and modular reconfiguration robust to temperature and tile concentration.

Two major issues that now limit the scalability of tile displacement systems are the purity of complex assemblies and occlusion between assemblies. Taking the sword as an example, more than

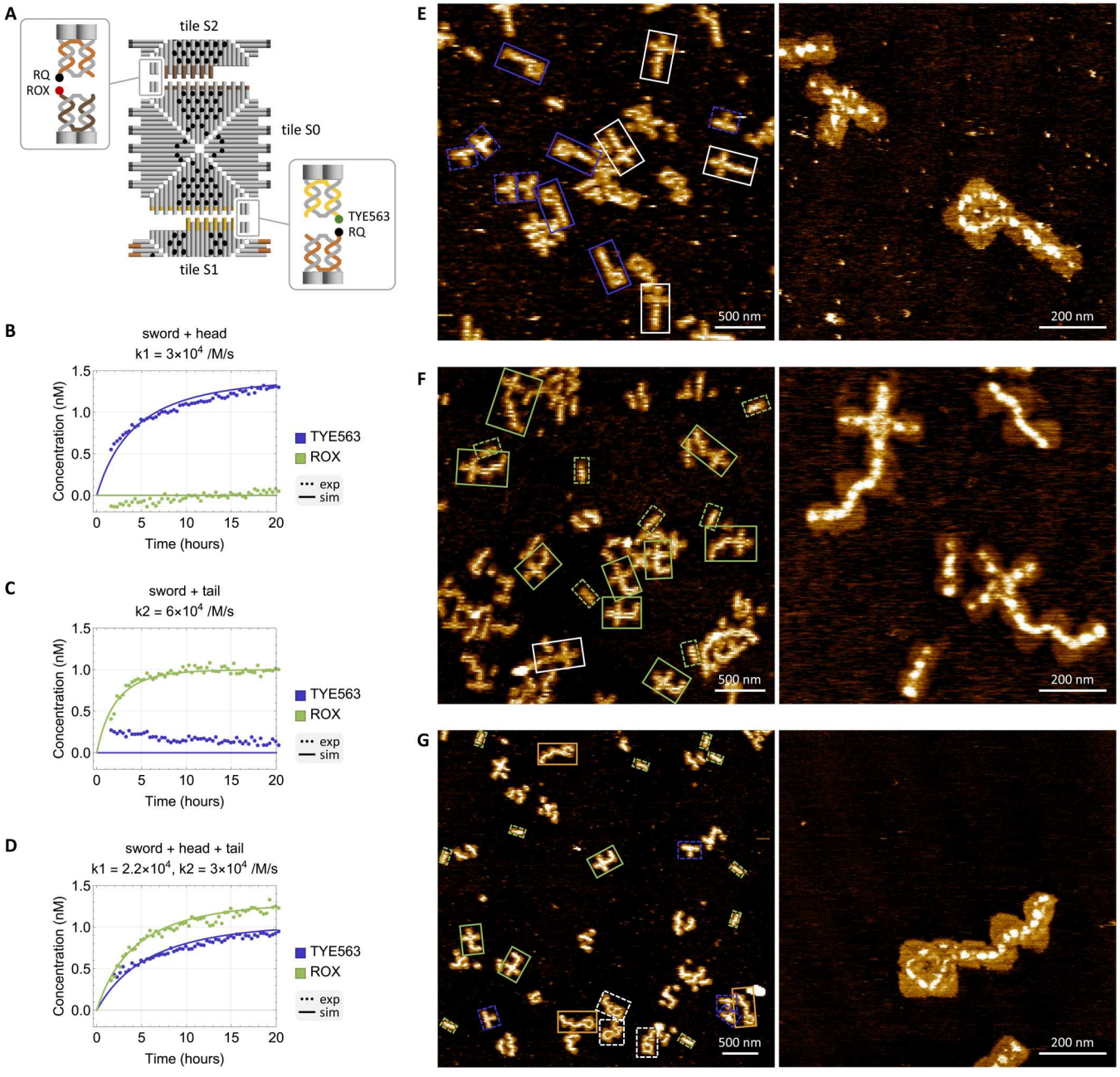

Fig. 8. Reconfiguration of sword to snake. (**A**) Quencher- and fluorophore-labeled edge staples. (**B** to **D**) Fluorescence kinetics data and simulation of the sword mixed with the head invader alone (B), the tail invader alone (C), or both invaders (D). Simulations and experiments are shown in solid and dotted trajectories, respectively. Experiments were performed at 25°C with the sword, head, and tail at 2, 2.4, and 2.4 nM, respectively. (**E** to **G**) AFM image of the sword mixed with the head invader alone (E), the tail invader alone (F), or both invaders (G). White and colored rectangles highlight the reactants and products of a tile displacement reaction, respectively. Solid and dotted blue rectangles highlight the head-blade and handle structures, respectively, both of which are products of the displacement reaction initiated by a head invader. Solid and dotted green rectangles highlight the handle-tail and blade structures, respectively, both of which are products of the displacement reaction initiated by a tail invader. Orange rectangles highlight the snake structure, which is the product of the two displacement reactions simultaneously initiated by the head and tail invaders. Dotted white rectangles highlight undesired products of spurious binding between the head and tail invaders.

50% of the structures were incomplete assemblies and aggregates. Given the size of the structures and the strength of the connections between tiles, it would be difficult to purify them on a gel (*24*). Other purification methods such as glycerol-gradient centrifugation (*34*) could be explored, although a better solution would be to develop more robust tile designs that can be successfully purified on a gel, for example, designs that have more compact structures and stronger tile-tile interactions while maintaining sufficient structural flexibility required for displacement. To effectively reduce occlusion between assemblies, we would move away from sequence complementarity and instead use shape complementarity (*5*, *18*, *19*) to program the interactions between tiles. Shape complementarity has been previously exploited in tile displacement systems in the form of edge codes, where distinct subsets of edge staples were left out to create empty space on an edge for defining its geometry (*16*). More generally, edges with various shapes can be created in single and multilayer DNA origami tiles, increasing the entropic barrier for spurious binding and further augmenting the design space of tile displacement reactions.

There is a trade-off between the structural flexibility of DNA origami tiles and the functionality of the circuits and motors attached to their surfaces. More flexible tile designs such as wireframe DNA origami structures (*35*, *36*) could help improve the rate and yield of tile displacement, especially in 3D reconfiguration tasks. On the other hand, the behaviors of spatially organized circuits and motors are more predictable with more rigid tile designs (*12*). This trade-off must be taken into consideration in future work on functionalizing tile displacement systems with circuits and motors. Moreover, in these systems, signal transduction across tiles could be affected by the intermediate states of tile displacement. A better understanding of the geometrical properties of the intermediate states could be achieved by locking branch migration at specific locations using photocrosslinking methods (*37*).

Conceptually, there is a gap between the type of self-reconfiguration task demonstrated here and the reconfigurable artificial cell envisioned at the beginning of this paper. The head and tail invaders were free-floating in the test tube rather than being "carried" by the sword, which means that the sword could only reconfigure itself into a snake if the head and tail structures were available as resources in the molecular environment. To develop artificial cells that incorporate the principle of modular reconfiguration, as seen in electromechanical robots, this stochasticity should be eliminated. To achieve that, an important next step is to develop localized tile displacement systems where an invader moves along the edges of a tile assembly and simultaneously reconfigures it, similar to how strand displacement takes place between localized components (*38*, *39*). Taking it further, catalytic invaders could be developed to enable self-reconfiguration in modular molecular machines where different parts of the system can be rearranged by the same invader whose activity (for example, turning on and off) is regulated by environmental stimuli.

Incorporating pervasive adaptability into future synthetic cells will likely require modular reconfiguration at multiple scales. Tile displacement operates at the level of DNA origami assemblies; it could be integrated with reconfiguration within individual tiles (*40*, *41*) to enable more efficient algorithms, such as those discussed in modular robots with expanding and contracting units (*42*). In contrast to a DNA-only approach, cell-scale robots with reconfiguration capabilities could also be created by using liposomes, microtubules, and protein motors (*43*). An open question is how the function of DNA origami tiles, which is determined not only by their structural properties but also by the information-processing circuits and motors attached to them, could benefit from the robustness and speed of protein motors (*44*, *45*).

In theory, tile displacement is Turing universal and can simulate arbitrary 2D synchronous block cellular automata (*46*), where each transition rule for updating the state of a two-by-two neighborhood is implemented by just a single tile (*47*). The ability of shape reconfiguration in tile displacement systems now opens up new theoretical questions about the algorithms and time complexity of reconfiguration from one shape to another using the same set of tiles, like what has been studied in the nubot model (*48*) and lattice-based modular robot models (*49*) but now with potential physical implementations using DNA origami tiles. Overall, we hope that the design principles established in this work will pave the way for future developments in tile displacement systems toward modular self-reconfiguration and dynamic self-reprogramming in artificial molecular machines.

MATERIALS AND METHODS

DNA oligonucleotides

Oligonucleotides were designed using the DTD designer (*50*). Giving edge staples contain a 2-nt extension on the 5′ end, the sequence of which was determined by the M13 scaffold sequence on the receiving edge. Receiving edge staples contain a 2-nt truncation on the 3′ end. Pattern staples have a 20-nt poly-adenine domain on the 3′ end. Fluorophore- and quencher-modified staples were high-performance liquid chromatography–purified, and other staples were unpurified (standard desalting). They were purchased from Integrated DNA Technologies at 100 μM in 1× TE buffer (10 mM tris-HCl and 1 mM EDTA) at pH 8.0 and stored in 384-well Echo source plates at 4°C. The scaffold strand was M13mp18 DNA (Bayou Biolabs, catalog number P-107), which varied in concentration within 5% of 0.375 μM. Negation strands were used to block excess edge staples from interacting with other tiles when different types of tiles were mixed together to assemble into larger structures; they were purchased unpurified and stored at 300 μM in 1× TE buffer.

Sample preparation

DNA origami tiles were annealed with 50 nM scaffold and 250 nM staples, with the exception of fluorophore- and quencher-modified staples, which were at 50 nM. The staple strands were mixed together using a Labcyte Echo 525 liquid handler and transferred into a 96-well destination plate with conical wells (Eppendorf, catalog number 951020401). The destination plate was centrifuged for 1 min at 2500 RCF (relative centrifugal field), the scaffold strand was added, and the final mixtures were prepared in 1× TE/Mg^{2+} buffer (1× TE, 12.5 mM Mg^{2+}). The samples were transferred into tubes and annealed in an Eppendorf Mastercycler thermocycler. They were held at 90°C for 2 min and then cooled from 90° to 20°C at 6 s per 0.1°C. Negation strands were added at 1.25 μM and then annealed from 50° to 20°C at 2 s per 0.1°C. Tile assemblies were created by mixing tiles together at ratios specified in the figures. For experiments using a cover:base dimer, the dimer was prepared with 20% excess of the CT. Tile assemblies were annealed

from 50° to 20°C at 2 min per 0.1°C and stored at −20°C when not in use.

Fluorescence spectroscopy

Fluorescent experiments were run in 1× TE/Mg^{2+} buffer in 384-well plates (black with clear flat bottom, polystyrene NBS, Corning 3651) on a monochromator-based plate reader (Synergy H1, Biotek), with a 45-μl reaction volume and data collected every 2 to 4 min. All experiments were run at 25°C. The concentrations for each experiment are specified in the figure captions. Excitation/emission wavelengths were 528/608 nm and 538/568 nm for ROX and TYE563, respectively. Each set of experiments was performed with a negative and a positive control, which were a reactant and an annealed product of the tile displacement reaction, respectively. Data were normalized using the average of the first five data points of the negative control as 0 and the average of the last five data points of the positive control as 2 nM (an example is shown in fig. S16). For experiments where kinetic trajectories had reached reaction completion within 24 hours, the average of the last five data points at 24 hours was used as 2 nM to normalize the data (this was done for experiments shown in Fig. 2B).

AFM imaging

Samples were diluted to 1/x nM, where x is the number of tiles in the assembly, in 1× TE/Mg^{2+} buffer. Forty microliters of the sample were deposited onto freshly cleaved 10-mm mica (Ted Pella, catalog number 50). Samples were washed twice with 1× TE/Mg^{2+} buffer and then twice with 1× TE buffer containing 10 mM $MgCl_2$ and 100 mM NaCl. Imaging was done in 80 μl of 1× TE/Mg^{2+} buffer on a FastScan Bio AFM (Bruker) in tapping mode using FastScan-D probes (Bruker). Images were collected at a scan rate of 5 Hz with 512 or 1024 lines per image, depending on the image size, and a drive frequency between 100 and 110 Hz.

Simulation

Simulations were performed with mass-action kinetics by solving ordinary differential equations using the CRN Simulator (*25*). Mathematica code for enumerating the reactions in growing a snake tail invader is available in an online repository (*51*).

Yield estimation

The yield of DNA origami assemblies was estimated as the total number of pixels in complete assemblies of the designed shape divided by the total number of pixels above the background threshold in AFM images. The estimation was facilitated by a software tool, the Yield Calculator (*52*).

Supplementary Materials

This PDF file includes:
Figs. S1 to S19
Tables S1 to S45

Other Supplementary Material for this manuscript includes the following:
MDAR Reproducibility Checklist
Mathematica code

REFERENCES AND NOTES

1. M. Yim, W. M. Shen, B. Salemi, D. Rus, M. Moll, H. Lipson, E. Klavins, G. Chirikjian, Modular self-reconfigurable robot systems [grand challenges of robotics]. *IEEE RObot. Autom. Lett.* **14**, 43–52 (2007).
2. P. W. Rothemund, Folding DNA to create nanoscale shapes and patterns. *Nature* **440**, 297–302 (2006).
3. A. E. Marras, L. Zhou, H.-J. Su, C. E. Castro, Programmable motion of DNA origami mechanisms. *Proc. Natl. Acad. Sci. U.S.A.* **112**, 713–718 (2015).
4. P. Ketterer, E. M. Willner, H. Dietz, Nanoscale rotary apparatus formed from tight-fitting 3D DNA components. *Sci. Adv.* **2**, e1501209 (2016).
5. T. Gerling, K. F. Wagenbauer, A. M. Neuner, H. Dietz, Dynamic DNA devices and assemblies formed by shape-complementary, non–base pairing 3D components. *Science* **347**, 1446–1452 (2015).
6. E. Kopperger, J. List, S. Madhira, F. Rothfischer, D. C. Lamb, F. C. Simmel, A self-assembled nanoscale robotic arm controlled by electric fields. *Science* **359**, 296–301 (2018).
7. E. Benson, R. C. Marzo, J. Bath, A. J. Turberfield, A DNA molecular printer capable of programmable positioning and patterning in two dimensions. *Robotics* **7**, eabn5459 (2022).
8. G. Chatterjee, N. Dalchau, R. A. Muscat, A. Phillips, G. Seelig, A spatially localized architecture for fast and modular DNA computing. *Nat. Nanotechnol.* **12**, 920–927 (2017).
9. K. Lund, A. J. Manzo, N. Dabby, N. Michelotti, A. Johnson-Buck, J. Nangreave, S. Taylor, R. Pei, M. N. Stojanovic, N. G. Walter, E. Winfree, H. Yan, Molecular robots guided by prescriptive landscapes. *Nature* **465**, 206–210 (2010).
10. H. Gu, J. Chao, S.-J. Xiao, N. C. Seeman, A proximity-based programmable DNA nanoscale assembly line. *Nature* **465**, 202–205 (2010).
11. S. F. Wickham, J. Bath, Y. Katsuda, M. Endo, K. Hidaka, H. Sugiyama, A. J. Turberfield, A DNA-based molecular motor that can navigate a network of tracks. *Nat. Nanotechnol.* **7**, 169–173 (2012).
12. A. J. Thubagere, W. Li, R. F. Johnson, Z. Chen, S. Doroudi, Y. L. Lee, G. Izatt, S. Wittman, N. Srinivas, D. Woods, E. Winfree, L. Qian, A cargo-sorting DNA robot. *Science* **357**, eaan6558 (2017).
13. S. Clamons, L. Qian, E. Winfree, Programming and simulating chemical reaction networks on a surface. *J. R. Soc. Interface* **17**, 20190790 (2020).
14. W. Liu, H. Zhong, R. Wang, N. C. Seeman, Crystalline two-dimensional DNA-origami arrays. *Angew. Chem. Int. Ed.* **50**, 264–267 (2011).
15. G. Tikhomirov, P. Petersen, L. Qian, Programmable disorder in random DNA tilings. *Nat. Nanotechnol.* **12**, 251–259 (2017).
16. P. Petersen, G. Tikhomirov, L. Qian, Information-based autonomous reconfiguration in systems of interacting DNA nanostructures. *Nat. Commun.* **9**, 5362 (2018).
17. B. Yurke, A. J. Turberfield, A. P. Mills Jr., F. C. Simmel, J. L. Neumann, A DNA-fuelled molecular machine made of DNA. *Nature* **406**, 605–608 (2000).
18. S. Woo, P. W. K. Rothemund, Programmable molecular recognition based on the geometry of DNA nanostructures. *Nat. Chem.* **3**, 620–627 (2011).
19. A. Rajendran, M. Endo, Y. Katsuda, K. Hidaka, H. Sugiyama, Programmed two-dimensional self-assembly of multiple DNA origami jigsaw pieces. *ACS Nano* **5**, 665–671 (2011).
20. N. E. Haley, T. E. Ouldridge, I. M. Ruiz, A. Geraldini, A. A. Louis, J. Bath, A. J. Turberfield, Design of hidden thermodynamic driving for non-equilibrium systems via mismatch elimination during DNA strand displacement. *Nat. Commun.* **11**, 2562–2511 (2020).
21. A. E. Brouwer, J. B. Shearer, N. J. Sloane, W. D. Smith, A new table of constant weight codes. *IEEE Trans. Inf.* **36**, 1334–1380 (1990).
22. G. Tikhomirov, P. Petersen, L. Qian, Triangular DNA origami tilings. *J. Am. Chem. Soc.* **140**, 17361–17364 (2018).
23. F. Schneider, N. Möritz, H. Dietz, The sequence of events during folding of a DNA origami. *Advances* **5**, eaaw1412 (2019).
24. G. Tikhomirov, P. Petersen, L. Qian, Fractal assembly of micrometre-scale DNA origami arrays with arbitrary patterns. *Nature* **552**, 67–71 (2017).
25. D. Soloveichik, CRNSimulator (2009); http://users.ece.utexas.edu/~soloveichik/crnsimulator.html.
26. S. M. Douglas, I. Bachelet, G. M. Church, A logic-gated nanorobot for targeted transport of molecular payloads. *Science* **335**, 831–834 (2012).
27. S. Li, Q. Jiang, S. Liu, Y. Zhang, Y. Tian, C. Song, J. Wang, Y. Zou, G. J. Anderson, J. Y. Han, Y. Chang, Y. Liu, C. Zhang, L. Chen, G. Zhou, G. Nie, H. Yan, B. Ding, Y. Zhao, A DNA nanorobot functions as a cancer therapeutic in response to a molecular trigger in vivo. *Nat. Biotechnol.* **36**, 258–264 (2018).
28. L. Qian, E. Winfree, Scaling up digital circuit computation with DNA strand displacement cascades. *Science* **332**, 1196–1201 (2011).
29. D. Y. Zhang, S. X. Chen, P. Yin, Optimizing the specificity of nucleic acid hybridization. *Nat. Chem.* **4**, 208–214 (2012).

30. K. M. Cherry, L. Qian, Scaling up molecular pattern recognition with DNA-based winner-take-all neural networks. *Nature* **559**, 370–376 (2018).
31. X. Xiong, T. Zhu, Y. Zhu, M. Cao, J. Xiao, L. Li, F. Wang, C. Fan, H. Pei, Molecular convolutional neural networks with DNA regulatory circuits. *Nat. Mach. Intell.* **4**, 625–635 (2022).
32. P. W. K. Rothemund, N. Papadakis, E. Winfree, Algorithmic self-assembly of DNA sierpinski triangles. *PLoS Biol.* **2**, e424 (2004).
33. D. Woods, D. Doty, C. Myhrvold, J. Hui, F. Zhou, P. Yin, E. Winfree, Diverse and robust molecular algorithms using reprogrammable DNA self-assembly. *Nature* **567**, 366–372 (2019).
34. C. Lin, S. D. Perrault, M. Kwak, F. Graf, W. M. Shih, Purification of DNA-origami nanostructures by rate-zonal centrifugation. *Nucleic Acids Res.* **41**, e40 (2013).
35. F. Zhang, S. Jiang, S. Wu, Y. Li, C. Mao, Y. Liu, H. Yan, Complex wireframe DNA origami nanostructures with multi-arm junction vertices. *Nat. Nanotechnol.* **10**, 779–784 (2015).
36. E. Benson, A. Mohammed, J. Gardell, S. Masich, E. Czeizler, P. Orponen, B. Högberg, DNA rendering of polyhedral meshes at the nanoscale. *Nature* **523**, 441–444 (2015).
37. S. Nakamura, H. Hashimoto, S. Kobayashi, K. Fujimoto, Photochemical acceleration of DNA strand displacement by using ultrafast DNA photo-crosslinking. *Chembiochem* **18**, 1984–1989 (2017).
38. M. Teichmann, E. Kopperger, F. C. Simmel, Robustness of localized DNA strand displacement cascades. *ACS Nano* **8**, 8487–8496 (2014).
39. H. Bui, S. Shah, R. Mokhtar, T. Song, S. Garg, J. Reif, Localized DNA hybridization chain reactions on DNA origami. *ACS Nano* **12**, 1146–1155 (2018).
40. F. Zhang, J. Nangreave, Y. Liu, H. Yan, Reconfigurable DNA origami to generate quasifractal patterns. *Nano Lett.* **12**, 3290–3295 (2012).
41. J. Song, Z. Li, P. Wang, T. Meyer, C. Mao, Y. Ke, Reconfiguration of DNA molecular arrays driven by information relay. *Science* **357**, eaan3377 (2017).
42. S. Vassilvitskii, J. Kubica, E. Rieffel, J. Suh, M. Yim, Proceedings 2002 IEEE International Conference on Robotics and Automation (IEEE, 2002), vol. 1, pp. 801–808.
43. Y. Sato, Y. Hiratsuka, I. Kawamata, S. Murata, S.-i. M. Nomura, Micrometer-sized molecular robot changes its shape in response to signal molecules. *Robotics* **2**, eaal3735 (2017).
44. J. J. Keya, R. Suzuki, A. M. R. Kabir, D. Inoue, H. Asanuma, K. Sada, H. Hess, A. Kuzuya, A. Kakugo, DNA-assisted swarm control in a biomolecular motor system. *Nat. Commun.* **9**, 1–8 (2018).
45. R. Ibusuki, T. Morishita, A. Furuta, S. Nakayama, M. Yoshio, H. Kojima, K. Oiwa, K. Furuta, Programmable molecular transport achieved by engineering protein motors to move on DNA nanotubes. *Science* **375**, 1159–1164 (2022).
46. T. Toffoli, N. Margolus, *Cellular Automata Machines: A New Environment for Modeling* (MIT Press, 1987).
47. E. Winfree, L. Qian, Two-dimensional tile displacement can simulate cellular automata. arXiv:2301.01929 (2023).
48. D. Woods, H. L. Chen, S. Goodfriend, N. Dabby, E. Winfree, P. Yin, Active self-assembly of algorithmic shapes and patterns in polylogarithmic time. arXiv:1301.2626 (2013).
49. G. Aloupis, N. Benbernou, M. Damian, E. D. Demaine, R. Flatland, J. Iacono, S. Wuhrer, Efficient reconfiguration of lattice-based modular robots. *Comput. Geom.* **46**, 917–928 (2013).
50. P. Petersen, DTD Designer (2018); http://qianlab.caltech.edu/DTDDesigner.
51. L. Qian, Snaketail invader simulation, Zenodo (2023); https://doi.org/10.5281/zenodo.7762398.
52. P. Petersen, Yield Calculator (2016); http://qianlab.caltech.edu/YieldCalculator.

Acknowledgments: We thank G. Tikhomirov, P. Petersen, and E. Winfree for discussions. We thank R. M. Murray for sharing an acoustic liquid handler. **Funding:** N.S., K.R.R., and L.Q. were supported by an NSF award (1813550). K.R.R. was also supported by a Bob and Carole Chapman Minority SURF fellowship. N.S. and L.Q. were also supported by a Schmidt Science Polymaths award. **Author contributions:** K.R.R. came up with a preliminary design of the system; N.S. designed and performed the experiments; all authors analyzed the data; N.S. and L.Q. wrote the manuscript; L.Q. initiated and guided the project. **Competing interests:** The authors declare that they have no competing interests. **Data and materials availability:** All data needed to support the conclusions of this manuscript are included in the main text or Supplementary Materials. The simulation code is available in an online repository: https://doi.org/10.5281/zenodo.7762398.

Submitted 2 October 2022
Accepted 28 March 2023
Published 26 April 2023
10.1126/scirobotics.adf1511

Science Robotics

Modular reconfiguration of DNA origami assemblies using tile displacement

Namita Sarraf, Kellen R. Rodriguez, and Lulu Qian

Sci. Robot., **8** (77), eadf1511.
DOI: 10.1126/scirobotics.adf1511